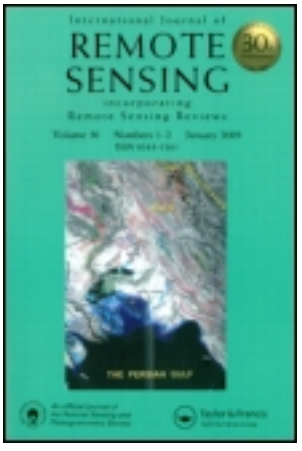

International Journal of Remote Sensing
Publication details, including instructions for authors and subscription information:
http://www.tandfonline.com/loi/tres20

Classification of multi-look polarimetric SAR imagery based on complex Wishart distribution

J. S. LEE [a], M. R. GRUNES [a] & R. KWOK [a]

[a] Code 7230, Remote Sensing Division, Naval Research Laboratory, Washington, DC, 20375-5351, U.S.A.

[b] Jet Propulsion Laboratory, California Institute of Technology, 4800 Oak Grove Drive, Pasadena, CA, 91109, U.S.A.

Version of record first published: 27 Apr 2007.

To cite this article: J. S. LEE, M. R. GRUNES & R. KWOK (1994): Classification of multi-look polarimetric SAR imagery based on complex Wishart distribution, International Journal of Remote Sensing, 15:11, 2299-2311

To link to this article: http://dx.doi.org/10.1080/01431169408954244

INT. J. REMOTE SENSING, 1994, VOL. 15, NO. 11, 2299–2311

Classification of multi-look polarimetric SAR imagery based on complex Wishart distribution

J. S. LEE, M. R. GRUNES

Code 7230, Remote Sensing Division, Naval Research Laboratory, Washington, DC 20375-5351, U.S.A.

and R. KWOK

Jet Propulsion Laboratory, California Institute of Technology, 4800 Oak Grove Drive, Pasadena, CA 91109, U.S.A.

(Received 26 March 1993; in final form 10 August 1993)

Abstract. Multi-look polarimetric SAR (synthetic aperture radar) data can be represented either in Mueller matrix form or in complex covariance matrix form. The latter has a complex Wishart distribution. A maximum likelihood classifier to segment polarimetric SAR data according to terrain types has been developed based on the Wishart distribution. This algorithm can also be applied to multi-frequency multi-look polarimetric SAR data, as well as to SAR data containing only intensity information. A procedure is then developed for unsupervised classification.

The classification error is assessed by using Monte Carlo simulation of multi-look polarimetric SAR data, owing to the lack of ground truth for each pixel. Comparisons of classification errors using the training sets and single-look data are also made. Applications of this algorithm are demonstrated with NASA/JPL *P*-, *L*- and *C*-band polarimetric SAR data.

1. Introduction

Classification of ground cover, such as forest, vegetation, sea-ice types, ocean and urban areas, has been an important application of polarimetric SAR (synthetic aperture radar) images. Some proposed classification schemes fail to utilize complete polarimetric information. These methods use only the intensities of HH, HV and VV, the phase difference between HH and VV, the ratio of $|HH|$ and $|VV|$ (Kwok *et al.* 1991, Du *et al.* 1992), or the coefficient of variation (van Zyl *et al.* 1987). One exception was the use of the multivariate complex Gaussian distribution of the three complex polarimetric components, HH, HV and VV, for Bayes classification by Kong *et al.* (1988) and Lim *et al.* (1989). They showed that the use of the full polarimetric data gives optimal classification results. However, the algorithm was only developed for application to single-look polarimetric SAR data.

For speckle reduction and data compression, SAR and polarimetric SAR data are frequently multi-look processed. Most notably, the JPL aircraft SAR processor compresses the polarimetric data into four-look images by averaging the Mueller matrices of four neighbouring azimuth pixels (Dubois and Norikane 1987). Recently, JPL devised a new frame processor (Garande *et al.* 1992), which processes raw data to sixteen-look polarimetric SAR data. Theoretically, it is impossible to recover completely the three complex polarimetric components (HH, HV, VV), because the phase of each component is lost when forming the Mueller matrix (only the phase differences are retained), and because the averaging of the Mueller matrix may introduce diffuse scattering components. The purpose of this paper is to

0143–1161/94 $10.00

develop an optimal classification scheme using the complete multi-look polarimetric SAR data, and to evaluate the classification errors both theoretically and practically.

Multi-look polarimetric SAR averaging can be performed using either the Mueller matrix or the complex covariance matrix. Since the elements of the 4×4 Mueller matrix are a linear combination of the elements in the 3×3 complex covariance matrix, the averaging process of either representation produces the same result. From our point of view, the advantage of using the covariance matrix is that its sample distribution has a multivariate complex Wishart distribution (Goodman 1963). In this paper, a maximum likelihood classifier is developed based on the complex Wishart distribution, using the complete multi-look polarimetric data in covariance matrix form. The generalization of this algorithm to include the case where only partial polarimetric SAR data are available is discussed, such as the processed data of the JPL synoptic processor (Taylor 1992) which produces only detected power images (i.e., no phase information is retained).

The Mueller matrix is converted first into the covariance matrix representation for each pixel. The pixel is then classified using the derived optimal discriminating function. The classes are defined by averaging pixels in training areas. In addition, a simple unsupervised classification without using training areas is developed. NASA/JPL compressed polarimetric SAR data of a land scene and a sea-ice scene are utilized for illustration.

To estimate the classification error, in the absence of detailed ground truth, a theoretical Monte Carlo procedure is applied. A multi-look polarimetric SAR data set is first simulated, then classified using the discriminating function for each class. The classification error is then assessed. This theoretical classification result is also compared with the practical classification result evaluated on the actual image by assuming that each training area is homogeneous. The theoretical difference in classification accuracies between single-look and multi-look classifiers is also investigated. Finally, the results are extended to multi-frequency classification, using NASA/JPL *P*-, *L*- and *C*-band compressed polarimetric SAR data.

2. Classification of single-look polarimetric SAR imagery

A polarimetric radar (van Zyl *et al.* 1987) measures the complete scattering matrix $\mathbf{S}$ of a medium at a given incidence angle. The scattering matrix with complex elements is given by

$$\mathbf{S} = \begin{bmatrix} S_{hh} & S_{hv} \\ S_{vh} & S_{vv} \end{bmatrix} \tag{1}$$

For a reciprocal medium, the relation $S_{hv} = S_{vh}$ is satisfied. The three unique elements define a complex vector:

$$\mathbf{u} = \begin{bmatrix} S_{hh} \\ S_{hv} \\ S_{vv} \end{bmatrix} \tag{2}$$

If it is desired that $\mathbf{u}$ satisfy $|\mathbf{u}|^2 = \text{span}$ (total power), S_{hv} should be weighted by $\sqrt{2}$. However, the distance measures to be derived in (7), (14) and (15) remain the same. In other words, the weighting of $\sqrt{2}$ does not change the classification result.

When the radar illuminates an area of a random surface of many elementary scatterers, $\mathbf{u}$ can be modelled as having a multivariate complex Gaussian distribution (Goodman 1963),

$$p(\mathbf{u}) = \frac{1}{\pi^3 |\mathbf{C}|} \exp\left(-\mathbf{u}^T C^{-1} \mathbf{u}\right) \tag{3}$$

where the complex covariance $\mathbf{C} = E[\mathbf{u}\mathbf{u}^T]$, T denotes the complex conjugate transpose, and $|\mathbf{C}|$ is the determinant of $\mathbf{C}$. The complex covariance matrix is Hermitian, i.e., $\mathbf{C} = \mathbf{C}^T$. We shall denote by CN(0, C) a complex normal distribution with zero mean and covariance C. Let $\mathbf{u}_j$ be an element of $\mathbf{u}$, $\mathbf{u}_j = x_j + iy_j$. The conditions (see Goodman 1963) for $\mathbf{u}$ to satisfy the complex Gaussian distribution are $E[x_j] = E[y_j] = 0$, $E[x_j^2] = E[y_j^2]$, $E[x_j y_j] = 0$, $E[x_j x_k] = E[y_j y_k]$, and $E[y_j x_k] = -E[x_j y_k]$.

Each class is characterized by its own covariance matrix. We shall call it the feature covariance matrix. The feature covariance $\mathbf{C}_m$ for the m^{th} class, ω_m, is estimated using training samples from ω_m. According to the Bayes maximum likelihood classification (Fukunaga 1972), a vector $\mathbf{u}$ is assigned to ω_m, if

$$P(\omega_m|\mathbf{u}) \geq P(\omega_j|\mathbf{u}), \quad \text{for all } j \neq m \tag{4}$$

Applying Bayes' rule of

$$P(\omega_m|\mathbf{u}) = \frac{p(\mathbf{u}|\omega_m)P(\omega_m)}{p(\mathbf{u})} \tag{5}$$

we have

$$\mathbf{u} \in \omega_m, \text{ if } p(\mathbf{u}|\omega_m)P(\omega_m) > p(\mathbf{u}|\omega_j)P(\omega_j), \quad \text{for all } j \neq m \tag{6}$$

where $p(\mathbf{u}|\omega_m)$ is CN(0, C_m), and $P(\omega_m)$ is the *a priori* probability of class ω_m. Kong *et al.* (1988) have derived a distance measure,

$$d_1(\mathbf{u}, \omega_m) = \mathbf{u}^T \mathbf{C}_m^{-1} \mathbf{u} + \ln|\mathbf{C}_m| - \ln[P(\omega_m)] \tag{7}$$

The feature vector $\mathbf{u}$ is assigned to class ω_m, if $d_1(\mathbf{u}, \omega_m) \leq d_1(\mathbf{u}, \omega_j)$, for all $j \neq m$.

Lim *et al.* (1989) also applied (7) for terrain classification based on multiple independent measurements by using the sum of each individual distance measure as the total distance measure. However, it was not clear that the multi-look Mueller matrix data were applied.

3. Multi-look polarimetric SAR data and the Wishart distribution

It has been mentioned in Section 1 that SAR data are frequently multi-look processed for speckle reduction and data compression, and that conversion from the averaged Mueller matrix to the covariance matrix produces results identical to averaging covariance matrices. The Mueller matrix, M, is a real 4×4 symmetrical matrix, and the elements of the covariance matrix are obtained by

$$\begin{aligned}
S_{hh}S_{hh}^* &= M_{11} + M_{22} + 2M_{12} \\
S_{hv}S_{hv}^* &= M_{11} - M_{22} \\
S_{vv}S_{vv}^* &= M_{11} + M_{22} - 2M_{12} \\
S_{hh}^*S_{hv} &= M_{13} + M_{23} + i(M_{14} + M_{24}) \\
S_{hv}^*S_{vv} &= M_{13} - M_{23} + i(M_{14} - M_{24}) \\
S_{hh}^*S_{vv} &= M_{33} - M_{44} + i2M_{34}
\end{aligned} \tag{8}$$

The Mueller matrix has a computational advantage over the covariance matrix in polarization synthesis. However, the covariance matrix has the distinct advantage in that it has a multivariate complex Wishart distribution.

Multi-look polarimetric SAR processing requires averaging several independent single-look covariance matrices, or

$$z=\frac{1}{n}\sum_{k=1}^{n}\mathbf{u}(k)\mathbf{u}(k)^T \tag{9}$$

where n is the number of look, and the vector $\mathbf{u}(k)$ is the k^{th} single-look sample.

Let

$$\mathbf{A}=nZ=\sum_{k=1}^{n}\mathbf{u}(k)\mathbf{u}(k)^T \tag{10}$$

The matrix $\mathbf{A}$ has a complex Wishart distribution. Goodman (1963) derived the complex Wishart distribution with the aid of characteristic functions and Fourier transforms. A simplified derivation was given by Srivastava (1965). The probability density function is

$$p(\mathbf{A})=\frac{|\mathbf{A}|^{n-q}\exp\left[-Tr(C^{-1}\mathbf{A})\right]}{K(n,q)|C|^n} \tag{11}$$

where $Tr(C^{-1}\mathbf{A})$ denotes the trace of $C^{-1}\mathbf{A}$, and

$$K(n,q)=\pi^{\frac{1}{2}q(q-1)}\Gamma(n)\ldots\Gamma(n-q+1) \tag{12}$$

The parameter q is the dimension of vector $\mathbf{u}$. For monostatic polarimetric SAR on a reciprocal medium, $q=3$. Goodman showed that Z is the maximum likelihood estimator of, and a sufficient statistic for, the covariance C.

4. Optimal classification based on the Wishart distribution

The Bayes maximum likelihood classifier is developed following the same procedure as for single-look polarimetric SAR. Substituting $\mathbf{C}_m$ for C, we can rewrite (11) as $p(\mathbf{A}|\omega_m)$. From (6) we maximize $p(\mathbf{A}|\omega_m)P(\omega_m)$, take the natural logarithm and change sign. We have a distance measure

$$d_2(\mathbf{A},\omega_m)=n\ln|\mathbf{C}_m|+Tr(\mathbf{C}_m^{-1}\mathbf{A})-\ln[P(\omega_m)]-(n-q)\ln|\mathbf{A}|+\ln[K(n,q)] \tag{13}$$

The last two terms can be eliminated, since they are not a function of ω_m, and do not contribute to the classification. Substituting (10) into (13), the distance measure for classification of n-look processed polarimetric SAR becomes

$$d_3(Z,\omega_m)=n[\ln|\mathbf{C}_m|+Tr(\mathbf{C}_m^{-1}Z)]-\ln[P(\omega_m)] \tag{14}$$

This indicates that as the number of looks, n, increases, the *a priori* probability $P(\omega_m)$ plays less of a role in the classification. For polarimetric SAR data with unknown proportions of each class, the $P(\omega_m)$ are assumed to be equal, in which case the distance measure is not a function of n. To implement the classification, the feature covariance, $\mathbf{C}_m$, is estimated using pixels within a selected training area of the m^{th} class, and data is then classified pixel by pixel. For each pixel, $d_3(Z,\omega_m)$ is computed for each class, and the class associated with the minimum distance is assigned to the pixel. This distance measure is simple and easy to apply. In addition, this algorithm uses the full polarimetric data.

5. Generalizations

The distance measure derived in the last section can be generalized to classify multi-frequency polarimetric SAR imagery and also detected-power polarization images:

(*a*) For multi-frequency polarimetric data, such as JPL AIRSAR with *P*, *L* and *C* bands, the distance measure of (14) can be extended by expanding the dimensions of $\mathbf{C}_m$ and Z. However, the increase in dimensionality prevents efficient computation. In practice, if the radar frequencies are sufficiently separated, the data is statistically independent between frequency bands. For example, NASA/JPL *P*-, *L*- and *C*-band AIRSAR data has been used by Lee & Hoppel (1992) to show that the correlations between bands were considerably less than those within bands. For statistically independent data, the joint probability density function is the product of the probabilities for each band, so the distance measure of (14) becomes

$$d_4(Z, \omega_m) = \sum_{j=1}^{J} n_j\{\ln|\mathbf{C}_m(j)| + Tr[\mathbf{C}_m(j)^{-1}Z(j)]\} - \ln[P(\omega_m)] \tag{15}$$

where $\mathbf{C}_m(j)$ is the feature covariance matrix of the m^{th} class in the j^{th} frequency band, $Z_{(j)}$ and n_j are a pixel's covariance matrix and the number of looks from the j^{th} frequency band, respectively, and J is the total number of bands. It should be noted that data from different bands should be properly co-registered.

(*b*) In many cases, several sets of SAR data of a scene are available, such as those from SIR-B with different look angles, and polarimetric SAR with only detected-power images. In addition, some SAR systems have limited recording capabilities, such as the NADC/ERIM SAR, which can only record four channels (e.g., *HH* and *VV* from *L* band, *VV* from C band and *VV* from *X* band). This algorithm can be adapted to all these situations. When only detected-power images are available, the off-diagonal terms of feature covariance matrices $\mathbf{C}_m$ and Z are set to zero, and then (14) or (15) is applied for classification. The algorithm remains the Bayes maximum likelihood classifier. For the aforementioned NADC/ERIM SAR with its limited recording capability, all the off-diagonal terms except the cross-correlation term between *HH* and *VV* from *L* band are set to zero. An example of using only detected-power images will be given in Section 7.

6. Theoretical estimation of classification accuracy

To evaluate the classification accuracy when ground truth is not available, theoretical classification errors can be calculated for a given set of $\mathbf{C}_m$ matrices by integrating the complex Wishart distributions. However, the difficulty in defining integration limits for each class means that this approach is not feasible. In this paper, we use a Monte Carlo procedure, which simulates multi-look polarimetric SAR pixels for each class. The number of pixels in each class is proportional to the *a priori* probability, $P(\omega_m)$. The classification scheme is then applied to estimate the classification accuracies. For the sake of completeness, the procedure of simulating a multi-look polarimetric SAR pixel is given in the Appendix.

7. Experimental results

Two datasets from NASA/JPL polarimetric SAR are used for illustration. The first set contains *L*-band four-look data from a San Francisco scene. A 512×512

pixel section of a pseudo-colour image (red for HH, green for HV, and Blue for VV) is shown in Figure 1 (*a*). The image is composed of mainly three classes, 'ocean', 'park' and 'city blocks'. The feature covariances $\mathbf{C}_m$, are computed using pixels from each training area, shown in rectangular boxes. Lim *et al.* (1989) reported difficulty in classifying 'ocean' pixels consistently, because the 'ocean' scattering mechanism varies with the incidence angle. We did not encounter this problem, because the selected training area on the top right of the image is different from that of Lim *et al.* However, difficulties arose in differentiating 'park' pixels from the coastal 'ocean' pixels, possibly due to surfactants in the coastal water. To overcome this difficulty, we added another 'ocean' class ('ocean 2'); as shown in the smaller rectangular box near the coast. Under the assumption of equal $P(\omega_m)$, the distance measure $d_3(Z, \omega_m)$ of (14) is applied to each class. The result is shown in figure 1(*b*). The colour assignments are white for 'city blocks', green for 'park', blue for 'ocean 1' and orange for 'ocean 2'. The use of two training areas for the 'ocean' has improved the ocean classification as compared to that of Lim *et al.* (1989). Some pixels of ball parks and grass areas are classified as ocean, because low-backscattering grass areas have a polarimetric signature similar to that of the ocean. To compensate for this problem, an additional class of 'quasi-natural surface' is created with training samples from the Golden Gate Park Stadium (polo field). The result is shown in figure 1 (*c*) with red pixels for 'quasi-natural surface'. This additional class solved this problem at the expense of a poorer classification of the coastal 'ocean' pixels ('ocean 2').

To show the importance of the phase and correlation information on the classification, only the three intensity (detected-power) images are used for classification with four classes, namely, 'city', 'park', 'ocean 1' and 'ocean 2'. The off-diagonal terms of $\mathbf{C}_m$ and Z are set to zero. The results, as shown in figure 1 (*d*) reveals that, in comparison with figure 1 (*b*), more pixels in the 'park' are classified as 'city', and a large number of 'ocean 1' pixels are classified as 'ocean 2'. This example substantiates the conclusion that full polarimetric information should be utilized for classification. More pixels in the 'park' are classified as 'city' because, in the city areas, more returns are characterized by double bounces, while 'park' areas are characterized by the diffused scattering. Hence phase differences between HH and VV of these two scattering mechanisms are different.

In addition to the theoretical estimation of classification accuracy using a Monte Carlo simulation, we also make a practical estimation. We assume that each training area belongs to a single class. In applications, the practical accuracy estimation will be lower than that of the theoretical estimation, because the training areas are actually inhomogeneous, especially in the city and the park areas. The results of this application are listed in table 1 for the four class classification as shown in figure 1 (*b*). Also included in the table is the theoretical result using single-look data. As expected, the theoretical result shows a higher correct classificatrion probability in every class, and four-look SAR data is much better in classification than single-look data. Table 2 shows the classification result with an additional class of 'quasi-natural surface'. This classification is somewhat inferior to the case of four classes.

The second set contains *P*-, *L*- and *C*-band four-look polarimetric SAR data for a sea-ice scene. This data is used for ice type classification. Ice classification using ERS-1 *C*-band VV SAR data has been investigated by Sun *et al.* (1992). For this study, it shows that the use of polarimetric data will improve the classification accuracy. A 512×512 pixel section of the total power image from three bands is

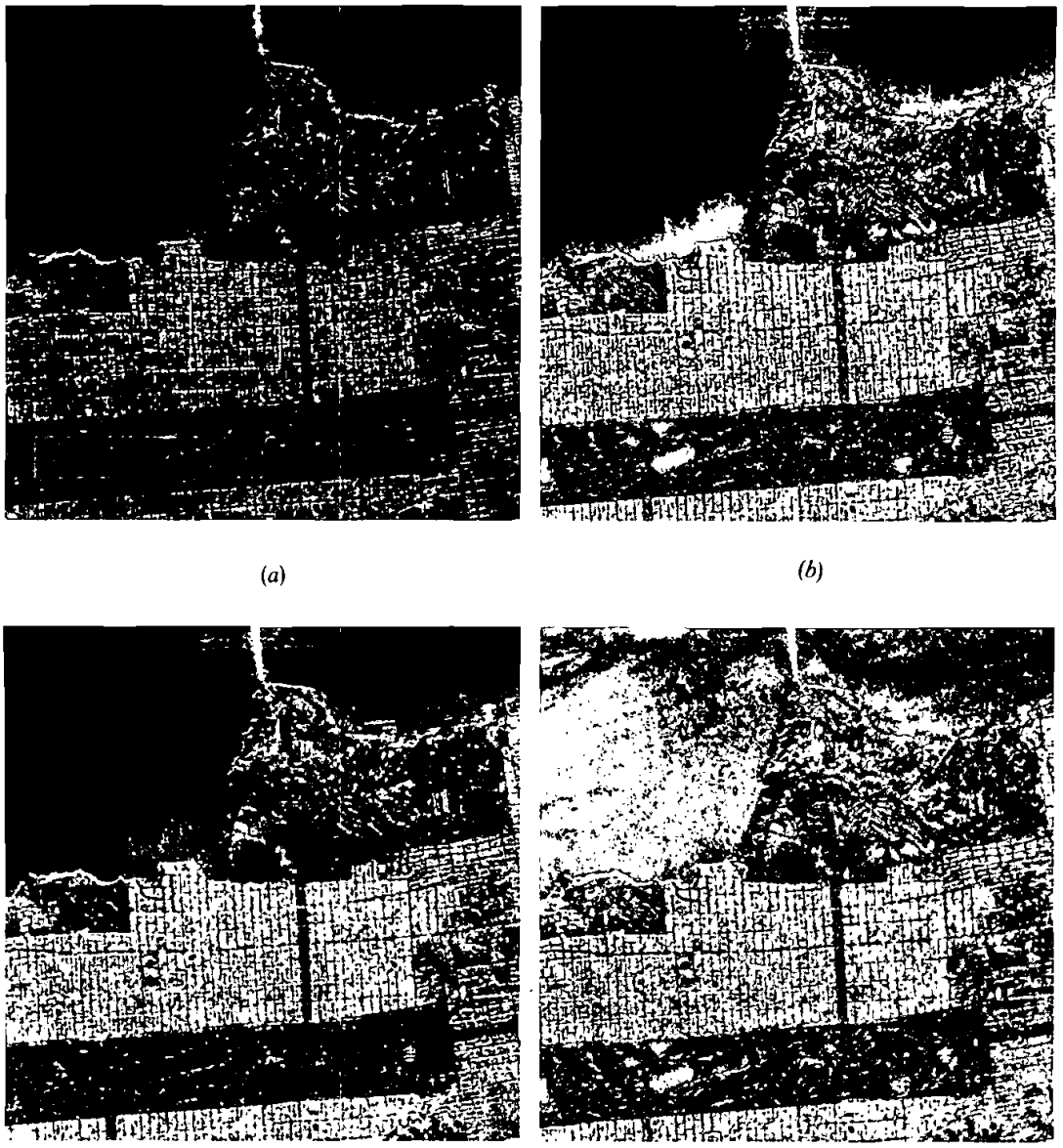

(*a*) (*b*)

(*c*) (*d*)

Figure 1. (*a*) Original image *L*-band San Francisco scene. Training areas are defined by boxes. Pseudo-colour: red = HH, green = HV, blue = VV. (*b*) Supervised classification based on the Wishart distribution. White = 'City', green = 'Park', blue = 'Ocean 1', orange = 'Ocean 2'. (*c*) Supervised classification with an additional class of quasi-natural ground cover, shown in red. (*d*) Supervised classification based on HH, HV and VV intensities only: no phase information is used.

Table 1. Probabilities of correct classification for four classes of San Francisco data. The practical estimation is obtained by using training areas, and the 4-look and 1-look theoretical estimations are obtained by using Monte Carlo simulation.

Class	Ocean 1	Ocean 2	Park	City	Total
Practical	90·9%	79·6%	78·2%	63·5%	78·0%
Theoretical (4-look)	97·5%	95·6%	99·0%	98·2%	97·6%
Theoretical (1-look)	87·4%	71·2%	84·4%	80·6%	80·9%

shown in figure 2(*a*) with red for P band, green for L band and blue for C band. Training areas are selected for four classes: first-year ice ('FY ice'), multi-year ice ('MY ice'), lead or 'open water' and 'ridge'. The box on the right of figure 2(*a*) contains MY ice pixels. The two smaller boxes in the upper left corner contain 'open water' and 'FY ice'. The large box nearby contains some 'ridge' pixels. Since there is no large uniform 'ridge' area, a threshold is used to establish a mask. Only those pixels above the threshold are considered as 'ridge' pixels for inclusion in the computation of C_m. The results of classification using each individual P, L and C band are shown in figures 2(*b*), (*c*) and (*d*), respectively. The colour assignments are black for 'open water', green for 'FY ice', orange for 'MY ice' and white for 'ridge'. The P and L bands exhibit difficulties in discriminating between 'open water' and 'FY ice', and the C band exhibits difficulty with 'MY ice' and 'ridge'. An artifact (vertical streak) shown in Figure 2(*d*) is due to defective C-band data. Overall, the L band produces the best classification of the three bands.

All three frequency bands are then combined using (15) for classification, as shown in figure 2(*e*). Considerable improvement over the results from individual bands is observed. All four classes are easily identified. When combining the frequency data, we found that the P band was not registered well with the L band and C bands. We have shifted the P-band data one pixel upward in the range direction for better co-registration.

Probabilities of correct classification using the training areas are listed in table 3. As expected, the P and L bands show difficulty in discriminating the 'FY ice' from the 'open water', while in the C band there is a problem identifying 'ridge'. The results using all three bands again show dramatic improvement over those for individual bands. The classification accuracy for all four classes is reasonably good, averaging 93·9 per cent correct. Theoretical results using the Monte Carlo simulation are presented in table 4 for comparison. It is interesting to note that the relative variations in classification probabilities are similar. For example, both tables show

Table 2. Probabilities of correct classification of San Francisco data with an additional class of 'quasi-natural surface' (lawn and stadium field).

Class	Ocean 1	Ocean 2	Park	City	Quasi-natural	Total
Practical	90·1%	64·6%	72·0%	63·5%	86·0%	75·2%
Theoretical (4-look)	97·2%	81·2%	99·0%	98·2%	87·1%	92·5%

(*a*)

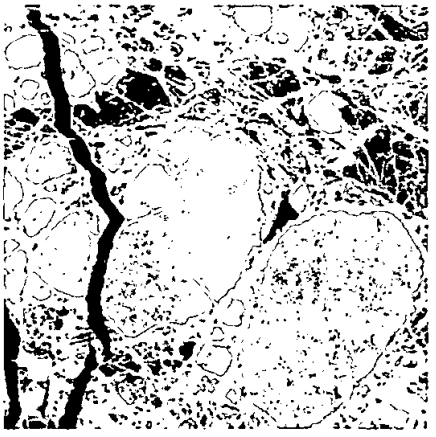

(*b*)

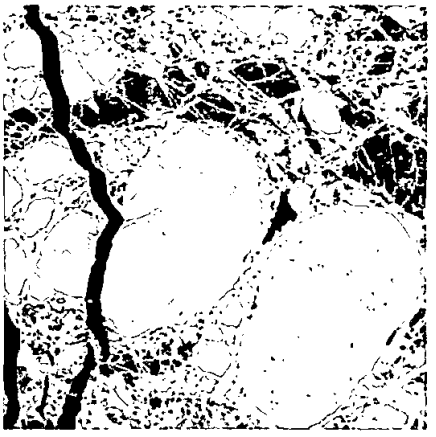

(*c*)

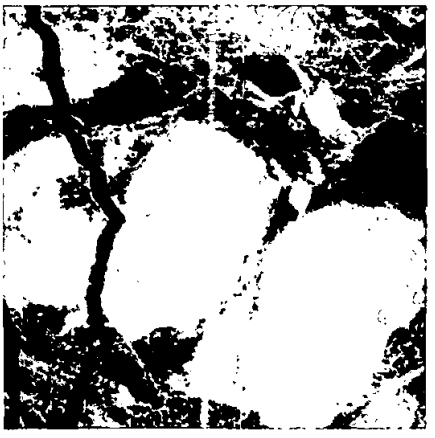

(*d*)

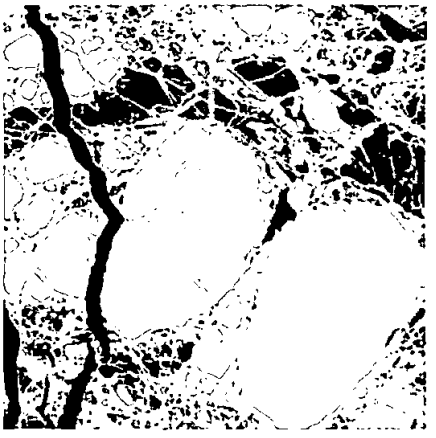

(*e*)

Figure 2. (*a*) Original sea-ice scene shown in total power form. Training areas are defined by boxes. Red = *P* band, green = *L* band, blue = *C* band. (*b*) Supervised ice classification, using *P* band. Black = Open water, green = FY ice, orange = MY ice, white = Ridge. (*c*) Supervised ice classification, using *L* band. (*d*) Supervised ice classification, using *C* band. (*e*) Supervised ice classification, using *P*, *L* and *C* bands.

that the P band has the lowest probability of correctly identifying 'FY ice', and that there is a problem in the C band with 'ridge'.

Additional measures could be used for separating two classes that are similar in C_m, such as 'ocean' and 'quasi-natural surface' in the first example. Since the ocean is characterized by a more significant decrease in temporal correlation than the quasi-natural surface, a time-domain interferometer should produce a more reliable classification.

8. Unsupervised classification of polarimetric SAR imagery

In unsupervised classifications, no training samples are required. Most unsupervised algorithms utilize clustering routines to find cluster centres. Most polarimetric SAR unsupervised techniques (e.g., Kwok *et al.* 1991) incorporate such a routine. A few exceptions, such as van Zyl (1989) and Lim *et al.* (1989), classify each pixel of the image by comparing its polarimetric properties to the various models of transmitting and receiving states. The distance measure derived in this paper can be incorporated in the ISODATA clustering algorithm (Bell and Hall 1974). Even though the ISODATA is intended to be an unsupervised algorithm, the parameters representing the minimum distance between class centre and the minimum size of each cluster have to be adjusted. In this paper, we tested an alternative approach. The distance measure of (14), and the feature covariance matrices, $\mathbf{C}_m$, (or the cluster centre) are iteratively updated from an initial estimate. The procedure and a simple proof of convergence of this algorithm were given by Swain and Davis (1978).

For most applications, rough estimates of the feature matrix of each class are frequently available. For example, in sea-ice classifications, the $\mathbf{C}_m$ matrices from a previous scene of the same band and from the same season can be utilized as an initial guess, even though the location and imaging geometry could be somewhat different. The procedure is listed as follows:

(*a*) Provide an initial $C_m^{(0)}$ as an initial guess for each class, $(k=0)$.
(*b*) Classify the whole image using (14) or (15) as the distance measure.
(*c*) Compute $C_m^{(k+1)}$ for each class using the classified pixels of step (*b*).
(*d*) Return to step (*b*), until a fixed number of iterations is reached, or the total distance between the cluster centres is larger than a given constant.

In our experiment, we used the feature covariances of the P band as the initial guess for the unsupervised classification using the L band of the sea-ice image. Figure 3(*a*) shows the initial classification of L-band data using P-band feature

Table 3. Practical estimation of probabilities of correct classification for the sea-ice scene. The P and L band are effective in distinguishing 'MY ice' and 'ridge', but are ineffective in discriminating 'open water' from 'FY ice'. The reverse is true for the C band. The combined P-, L-, C-band data shows its overall superiority in classification for all classes.

Class	Open water	FY ice	MY ice	Ridge	Total
P band	86·0%	41·7%	87·5%	99·0%	78·6%
L band	90·4%	60·2%	92·0%	100%	85·7%
C band	92·3%	84·8%	89·2%	55·7%	80·5%
P, L, C bands	95·8%	80·8%	99·2%	99·9%	93·9%

Table 4. Theoretical estimation of probability of correct classification of the sea-ice scene.

Class	Open water	FY ice	MY ice	Ridge	Total
P band	91·1%	84·4%	95·6%	100%	92·8%
L band	94·2%	89·7%	99·0%	100%	95·7%
C band	95·6%	91·6%	96·9%	94·7%	94·7%
P, *L*, *C* band	99·5%	99·0%	100%	100%	99·5%

covariance matrices, $\mathbf{C}_m$. The initial classification result is not good. After one iteration, however, the classification improved greatly as shown in figure 3(*b*). It is almost identical to the supervised classification as shown in figure 2(*c*). The improvement continued for classifying the 'MY ice' and 'FY ice' in the second and fourth iterations (figures 3*c* and *d*). Compared with the supervised classification of the *L* band (figure 2*c*), some minor differences were observed. The unsupervised

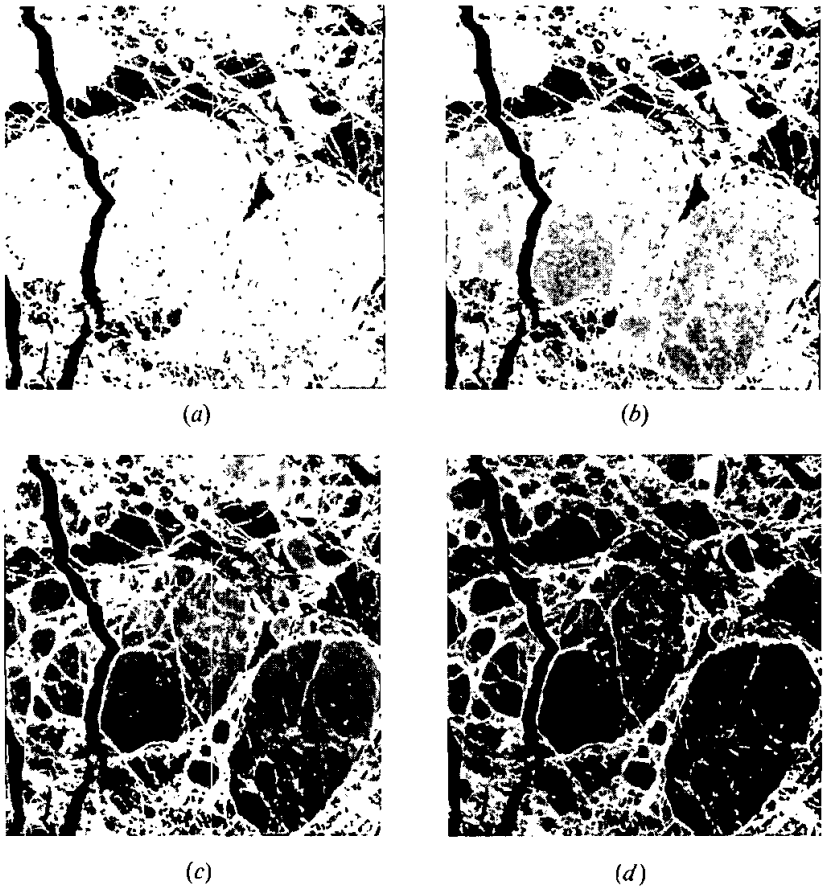

Figure 3. Results of unsupervised classification of sea ice using L-band polarimetric SAR data. (*a*) Initial classification. Black = 'open water', Grey = 'FY ice', Light Grey = 'MY ice', White = 'ridge'. (*b*) Classification after one iteration. (*c*) Classification after two iterations. (*d*) Classification after four iterations.

results showed more details and inhomogeneities, especially in the 'MY ice' regions. However, the theoretical estimate of correct classification probabilities showed a higher classification accuracy, with a total of 97·2 per cent, indicating that the total distances between the four cluster centres are larger than those of the supervised classification. This example shows that the unsupervised algorithm may improve the classification results.

9. Conclusion

We have developed terrain classification algorithms based on a complex Wishart distribution tailored to multi-look polarimetric SAR images. The classification is based on the complex covariance matrix, and utilizes the complete polarimetric data. We showed that as the number of looks increases, the *a priori* probability of each class becomes less important. The algorithm is then generalized to multi-frequency polarimetric SAR, and to SAR data containing only intensities. Classification errors were estimated using a Monte Carlo procedure, and compared with estimates using training areas as homogeneous regions. Applications of this algorithm were demonstrated using NASA/JPL compressed multi-look polarimetric SAR data.

Appendix

This appendix describes a procedure for simulating multi-look polarimetric SAR data:

(*a*) For each C_m, compute $C_m^{1/2}$, where

$$C_m^{1/2}(C_m^{1/2})^T = C_m \tag{A 1}$$

(*b*) Simulate a complex random vector $\mathbf{v}$ that is $CN(0, \mathbf{I})$, where $\mathbf{I}$ is an identity matrix. This can be easily accomplished by independently generating the real and imaginary components of each complex element of $\mathbf{v}$ with a normal distribution having mean zero and variance $\frac{1}{2}$.

(*c*) Compute $\mathbf{u} = C_m^{1/2}\mathbf{v}$. The complex vector $\mathbf{u}$ has $\mathrm{CN}(0, C_m)$, i.e., $\mathbf{u}$ is a single-look SAR pixel.

(*d*) Compute an n-look polarimetric SAR pixel by using (9).

This procedure can be easily verified, since

$$E[\mathbf{u}\mathbf{u}^T] = C_m^{1/2} E[vv^T](C_m^{1/2})^T = C_m \tag{A 2}$$

The complex matrix $\mathbf{C}_m^{1/2}$ is computed using an orthogonal transform Θ, whose columns are the eigenvectors of $\mathbf{C}_m$. The $\mathbf{C}_m$ is diagonalized by $\Theta^T\mathbf{C}_m\Theta = \Lambda$. The diagonal matrix Λ contains the eigenvalues (which are real) of $\mathbf{C}_m$. Taking the square root of each diagonal element of Λ, we have $\Lambda^{1/2}$. Finally, $\mathbf{C}_m^{1/2} = \Theta\Lambda^{1/2}$. A procedure for computing the eigenvalues and eigenvectors of a complex matrix can be found in Press (1986).

Acknowledgment

We wish to acknowledge the anonymous reviewers for their helpful comments.

References

Bell, G. H., and Hall, D. J., 1974, A clustering technique for summarizing multi-variate data, *Behavior Science*, **12**, 153–155.

Du, L., Lee, J. S., and Mango, S. A., 1992, Texture segmentation of SAR images using the wavelet transform. *Proceedings of 1992 International Geoscience and Remote Sensing*

Symposium (IGARSS'92) (New York: The Institute of Electrical and Electronics Engineers, Inc.), pp. 1108–1110.

DUBOIS, P. C., and NORIKANE, L., 1987, Data volume reduction for imaging radar polarimetry. *Proceedings ov 1987 International Geoscience and Remote Sensing Symposium (IGARSS'87)* (New York: The Institute of Electrical and Electronics Engineers, Inc.), pp. 691–696.

FUKUNAGA, K., 1972, *Introduction to Statistical Pattern Recognition* (San Diego, California: Academic Press).

GARANDE, R., CHAPMAN, B., LOU, Y., and TAYOR, V., 1992, JPL AIRSAR processing activities and developments. *Proceedings of 1992 International Geoscience and Remote Sensing Symposium (IGARSS'92)* (New York: The Institute of Electrical and Electronics Engineers, Inc.), pp. 1152–1154.

GOODMAN, N. R., 1963, Statistical analysis based on a certain multivariate complex Gaussian distribution (An Introduction), *Annals of Mathematical Statistics*, **34**, 152–177.

KONG, J. A., SWARTZ, A. A., YUEH, H. A., NOVAK, L. M., and SHIN, R. T., 1988, Identification of terrain cover using the optimal polarimetric classifier, *Journal of Electromagnetic Waves and Applications*, **2**, 171–194.

KWOK, R., *et al.*, 1991, Application of neural network to sea ice classification using polarimetric SAR images. *Proceedings of 1991 International Geoscience and Remote Sensing Symposium (IGARSS'91)* (New York: The Institute of Electrical and Electronics Engineers, Inc.), pp. 85–88.

LEE, J. S., and HOPPEL, K., 1992, Principal components transformation of multifrequency polarimetric SAR imagery. *IEEE Transactions on Geoscience and Remote Sensing*, **30**, 686–696.

LIM, H. H., *et al.*, 1989, Classification of earth terrain using polarimetric synthetic aperture radar images. *Journal of Geophysical Research*, **94**, 7049–7057.

PRESS, W. H., FLANNERY, B. P., TEUKOLSKY, S. A., and VETTERLING, W. T., 1986, *Numerical Recipes: The Art of Scientific Computing* (Cambridge: Cambridge University Press).

SRIVASTAVA, M. S., 1965, On the complex Wishart distribution, *Annals of Mathematical Statistics*, **36**, 313–315.

SUN, Y., CARLSTROM, A., and ASKNE, J., 1992, SAR image classification of ice in the Gulf of Bothnia, *International Journal of Remote Sensing*, **13**, 2049–2514.

SWAIN, P. H., and DAVIS, S. M., 1978, *Remote Sensing: The Quantitative Approach* (New York: McGraw-Hill, Inc.).

TAYLOR, V. B., 1992, CYLOPS: The JPL AIRSAR synoptic processor, *Proceedings of 1992 International Geoscience and Remote Sensing Symposium (IGARSS'92)* (New York: The Institute of Electrical and Electronic Engineers, Inc.), pp. 652–654.

VAN ZYL, J. J., ZEBKER, H. A., and ELACHI, C., 1987, Imaging radar polarimetric signatures: theory and observation. *Radio Science*, **22**, 529–543.

VAN ZYL, J. J., 1989, Unsupervised classification of scattering behavior using radar polarimetric data. *I.E.E.E. Transactions on Geoscience and Remote Sensing*, **27**, 36–45.